Cobalt Hydroxide/Oxide Hexagonal Ring–Graphene Hybrids through Chemical Etching of Metal Hydroxide Platelets by Graphene Oxide: Energy Storage Applications

C. Nethravathi,[†,*] Catherine R. Rajamathi,[‡] Michael Rajamathi,[‡,*] Xi Wang,[†,*] Ujjal K. Gautam,[§] Dmitri Golberg,[†,*] and Yoshio Bando[†]

[†]World Premier International (WPI) Center for Materials Nanoarchitectonics (MANA), National Institute for Materials Science (NIMS), Namiki 1-1, Tsukuba, Ibaraki 305-0044, Japan, [‡]Materials Research Group, Department of Chemistry, St. Joseph's College, 36 Lalbagh Road, Bangalore 560 027, India, and [§]New Chemistry Unit, Jawaharlal Nehru Centre for Advanced Scientific Research, Bangalore 560 064, India

ABSTRACT The reaction of β-$Co(OH)_2$ hexagonal platelets with graphite oxide in an aqueous colloidal dispersion results in the formation of β-$Co(OH)_2$ hexagonal rings anchored to graphene oxide layers. The interaction between the basic hydroxide layers and the acidic groups on graphene oxide induces chemical etching of the hexagonal platelets, forming β-$Co(OH)_2$ hexagonal rings. On heating in air or N_2, the hydroxide hybrid is morphotactically converted to porous Co_3O_4/CoO hexagonal ring–graphene hybrids. Porous $NiCo_2O_4$ hexagonal ring–graphene hybrid is also obtained through a similar process starting from β-$Ni_{0.33}Co_{0.67}(OH)_2$ platelets. As electrode materials for supercapacitors or lithium-ion batteries, these materials exhibit a large capacity, high rate capability, and excellent cycling stability.

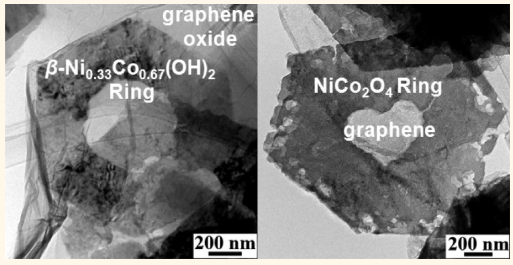

KEYWORDS: β-$Co(OH)_2$ hexagonal ring · graphene oxide · graphene hybrid · supercapacitor · lithium-ion battery

Nanostructures of unusual shapes associated with interesting properties have been of continued interest.[1−7] Among the unusual nanostructures, nanorings of metals[8−17] (Ag, Au, Au–Ag alloy, Pt, Ni, Co, Ni–Co alloy), oxides[18−26] (ZnO, CuO, TiO_2, $Ag_2V_4O_{11}$, $K_2Ti_6O_{13}$, α-Fe_2O_3, Fe_3O_4, Gd_2O_3, In_2O_3, Zn_2GeO_4), nitrides[27,28] (AlN, GaN), chalcogenides[29−36] (CdS/Se, Sb_2S_3, Sb_2Te_3, PbS/Se, $CuInSe_2$, Cu-$NaInSe_2$), carbon,[37] fullerene (C_{70}),[38] and $Cd(OH)_2$[39,40] have been explored and found to exhibit different properties in comparison to their counterparts of different shapes. For example, in the case of magnetic nanorings, the unique geometrical configuration governs the movement of a magnetic moment around the loop structure. By virtue of the stable vortex state possessed by the magnetic rings,[15,24,41,42] these have been proposed to be potential materials for magnetic random access memory[43] and as magnetic resonance imaging (MRI) contrasting agents.[17] In Au nanorings, uniform field enhancement effect has been observed in their cavities, and hence, they could potentially serve as resonant nanocavities to accommodate or probe smaller nanostructures in sensing and spectroscopy applications.[44]

The nanorings are known to form due to self-assembly of nanoparticles[19,29,30,38] or coiling of nanotubes,[45] nanobelts,[21,22,28,46] or nanowires.[26,27] These have generally been prepared by template-assisted synthesis,[8,20] thermal treatment,[32] lithography,[12,14] solvothermal reaction,[17,19,21,23,24] solution synthesis accompanied by chemical etching[23,24]/ion exchange,[36] or by galvanic displacement reactions.[9,11] Solution synthesis of nanorings has been demonstrated to be a facile and scalable route. In solution synthesis, one of the reactants usually acts as a chemical etchant. For instance, the addition of $HAuCl_4$ to a dispersion of Ag nanoplates causes galvanic displacement of Ag by Au, yielding Au nanorings.[9,11] Initially formed

* Address correspondence to nethravathic@gmail.com, mikerajamathi@rediffmail.com, wang.xi2@nims.go.jp, golberg.dmitri@nims.go.jp.

Received for review December 18, 2013 and accepted February 16, 2014.

Published online February 17, 2014
10.1021/nn406480g

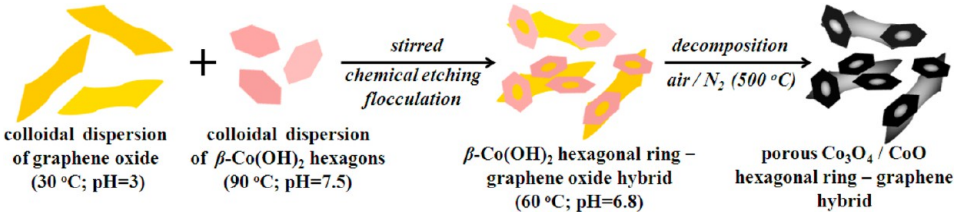

Figure 1. Schematic representation of the processes involved in the synthesis of Co_3O_4/CoO hexagonal ring−graphene hybrids.

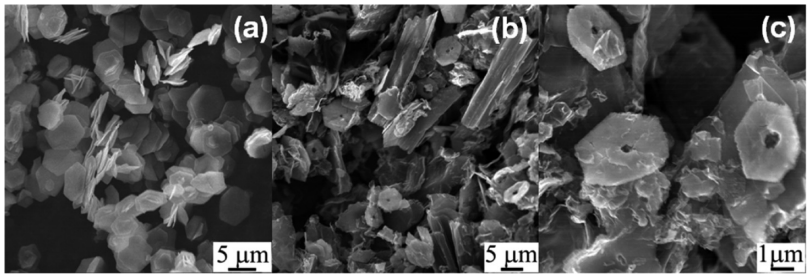

Figure 2. SEM images of β-Co(OH)$_2$ hexagonal platelets (a) and the β-Co(OH)$_2$ hexagonal ring−graphene oxide hybrid (b,c).

PbS nanoprisms are slowly etched to nanorings by Cl^- ions in solution.[34] Phosphate and sulfate ions play a key role in the formation of α-Fe_2O_3 nanorings.[24] While the phosphate ions regulate the shape of the nanorings, hollowing of the α-Fe_2O_3 structure is caused by preferential dissolution due to the coordinating sulfate ions.

Nanorings of layered metal hydroxides have not been well-explored. The fact that nanoplatelets or disks of metals,[9−11] oxides,[18,24] and chalcogenides[32,34,36] can be chemically etched to nanorings suggests that it should be possible to etch preformed nanoplatelets of layered metal hydroxides by a simple acid−base reaction using a mild acid as an etchant. Can mildly acidic graphite oxide (GO) layers be used as etchants? Though it has been well-established that the polar oxygen bearing functional groups of GO assist in solubilizing carbon layers and contribute to acidity (due to −OH and −COOH groups),[47−49] only recently it was demonstrated that they also play a crucial role in nucleation and growth of nanomaterials.[50−52] Though there has been a plethora of studies where nanomaterial is formed in the presence of GO during chemical reactions, studies on the interaction of GO with preformed nanomaterial is limited. It would be interesting to examine as to how the acidic functional groups on GO interact with preformed nanomaterials like hexagonal platelets of layered metal hydroxides. Using GO as a chemical etchant would lead to the formation of a layered metal hydroxide nanoring−GO hybrid which can eventually be converted to a metal oxide nanoring−graphene hybrid. The formation of nanorings on graphene would increase the overall exposed surface area since the inner edges of the nanorings along with graphene would also be available for catalytic activity.[53] These factors could be advantageous since hybridization of a functional nanomaterial with high surface area, conducting, and lightweight graphene has been explored as an effective strategy for enhanced catalysis in energy conversion and storage.[51−54]

In this article, we report the interaction between colloidal dispersion of cobalt hydroxide hexagonal platelets and aqueous colloidal dispersion of GO that induces chemical etching of the cobalt hydroxide hexagonal platelets resulting in the formation of cobalt hydroxide hexagonal rings. The cobalt hydroxide hexagonal ring−GO hybrid could be morphotactically converted to porous Co_3O_4/CoO ring−graphene hybrids, which were examined as anode materials for lithium-ion battery application. $NiCo_2O_4$ hexagonal ring−graphene hybrid prepared by a similar process was examined for supercapacitor application.

RESULTS AND DISCUSSION

The processes involved in the synthesis of Co_3O_4/CoO hexagonal ring−graphene hybrids are schematically depicted in Figure 1. The as-prepared β-Co(OH)$_2$ has hexagonal platelet morphology. The low-magnification SEM image of β-Co(OH)$_2$ (Figure 2a) shows uniform hexagonal platelets with a diameter of ∼5 μm and a thickness of ∼15 nm. On reacting with GO, these platelets are converted into hexagonal rings due to the etching out of the central part of the platelet by the acidic functional groups of GO. The SEM images of the β-Co(OH)$_2$ hexagonal ring−GO hybrid (Figure 2b,c) reveal the presence of β-Co(OH)$_2$ hexagonal rings randomly distributed within the corrugated GO layers.

Bright-field TEM images of the β-Co(OH)$_2$ hexagonal ring−GO hybrid (Figure 3a,b) show hexagonal rings present on GO layers. The inner diameter of the ring is ∼500 nm. The selected area electron diffraction (SAED) pattern obtained from an individual hexagonal ring of brucite-like β-Co(OH)$_2$ (Figure 3b inset) could be indexed to the [001] zone axis pattern. The hexagonally

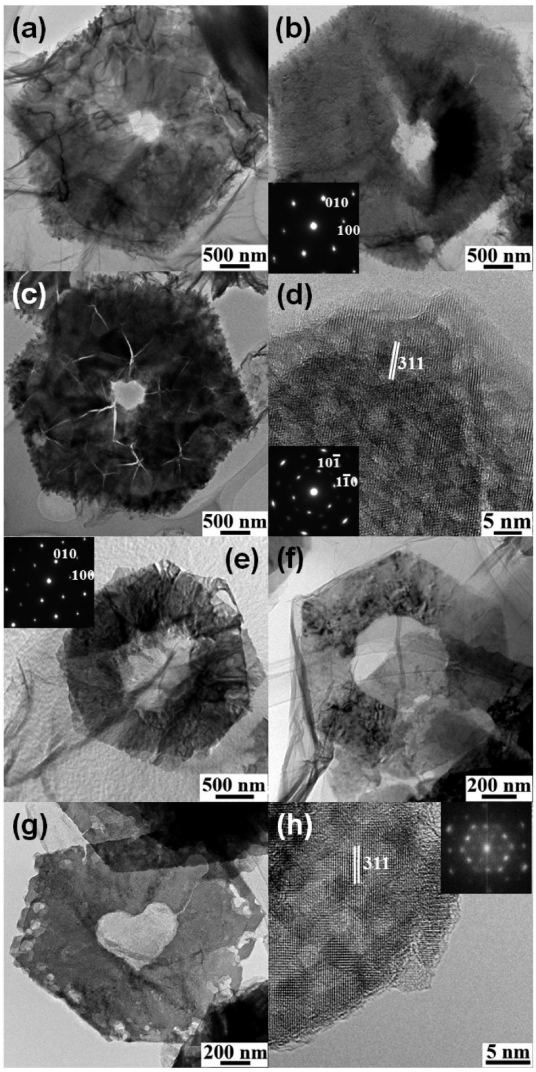

Figure 3. Bright-field TEM images of β-Co(OH)$_2$ hexagonal ring−graphene oxide (a,b), Co_3O_4 hexagonal ring−graphene (c), β-$Ni_{0.33}Co_{0.67}(OH)_2$ hexagonal ring−graphene oxide (e,f), and $NiCo_2O_4$ hexagonal ring−graphene (g) hybrids. HRTEM images of Co_3O_4 hexagonal ring−graphene (d) and $NiCo_2O_4$ hexagonal ring−graphene (h) hybrids.

arranged sharp diffraction spots suggest that the β-Co(OH)$_2$ rings are crystalline. On heating in air, β-Co(OH)$_2$ hexagonal rings of the β-Co(OH)$_2$ hexagonal ring−GO hybrid decompose morphotactically to Co_3O_4 rings, and GO in the hybrid is reduced to graphene. TEM image of the Co_3O_4 hexagonal ring−graphene hybrid thus formed (Figure 3c) shows a Co_3O_4 hexagonal ring with a number of cracks and a rough surface in contrast to the smooth β-Co(OH)$_2$ hexagonal rings seen in Figure 3a,b. The porous nature of the Co_3O_4 hexagonal rings is shown in the high-magnification images (Supporting Information, Figure S1). The lattice fringes observed in the HRTEM image of the Co_3O_4 hexagonal ring correspond to (311) lattice planes of Co_3O_4. The SAED pattern (Figure 3d inset) of the Co_3O_4 hexagonal ring on graphene corresponds to the [111] zone axis. This is in line with the observation

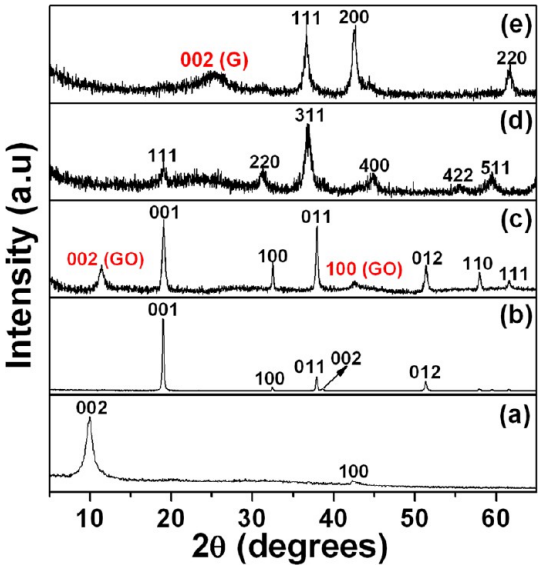

Figure 4. XRD patterns of pristine GO (a), pristine β-Co(OH)$_2$ hexagonal platelets (b), β-Co(OH)$_2$ hexagonal ring−GO hybrid (c), Co_3O_4 hexagonal ring−graphene hybrid (d), and CoO hexagonal ring−graphene hybrid (e).

made by Ma *et al.* that the conversion of hexagonal cobalt hydroxide platelets to Co_3O_4 is quasitopotactic.[55] Similarly, heating the β-Co(OH)$_2$ hexagonal ring−GO hybrid in nitrogen atmosphere results in porous CoO hexagonal ring−graphene hybrid (Supporting Information, Figure S2).

Similar results were obtained when β-$Ni_{0.33}Co_{0.67}(OH)_2$ hexagonal platelets were treated with GO though the platelets in this case were much smaller (~2 μm in diameter). Etching of the hexagonal hydroxide platelets seems to be more pronounced in β-$Ni_{0.33}Co_{0.67}$-(OH)$_2$ hexagonal rings−GO hybrid (Figure 3e,f) due to the smaller width (~2 μm) of the precursor platelets. This hybrid was converted to $NiCo_2O_4$ hexagonal ring −graphene hybrid on heating in air. As in the case of the Co_3O_4 hybrid, cracks and pores were developed in the $NiCo_2O_4$ hexagonal rings (Figure 3g). The HRTEM image (Figure 3h) shows lattice fringes due to (311) planes. The SAED patterns (shown as insets in Figure 3e,h) of an individual β-$Ni_{0.33}Co_{0.67}(OH)_2$ hexagonal ring on GO and $NiCo_2O_4$ hexagonal ring on graphene could be indexed to [001] and [111] zone axis patterns, respectively. Well-defined hexagonal diffraction spots indicate that the hexagonal rings in both cases are crystalline.

The XRD pattern of the β-Co(OH)$_2$ hexagonal ring−GO hybrid (Figure 4c) shows Bragg reflections due to both GO and β-Co(OH)$_2$. There are small changes in the Bragg reflections compared to the starting components (Figure 4a,b). The basal spacing of the GO component in the hybrid reduces to 7.7 Å (Figure 4c) from 9.0 Å observed for the precursor GO (Figure 4a), possibly due to partial reduction and reduced interlayer water. The peaks due to β-Co(OH)$_2$

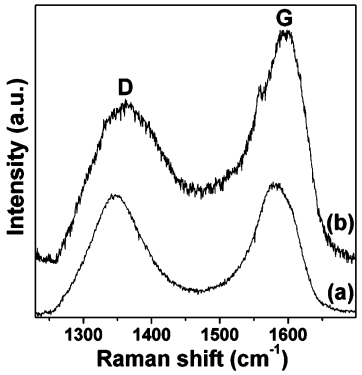

Figure 5. Raman spectra of β-Co(OH)$_2$ hexagonal ring−GO (a) and Co_3O_4 hexagonal ring−graphene (b) hybrids.

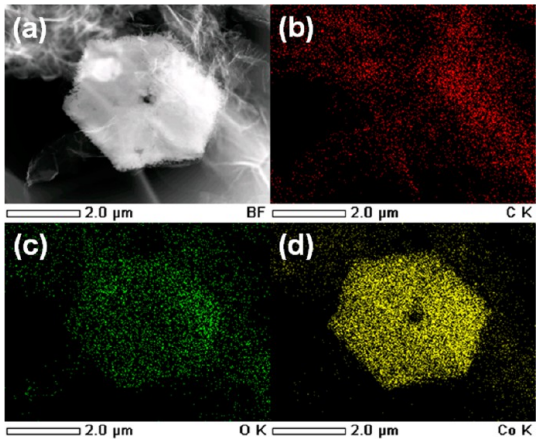

Figure 6. HAADF STEM image (a) and the spatially resolved C (b), O (c), and Co (d) elemental maps of the β-Co(OH)$_2$ hexagonal ring−GO hybrid.

(JCPDS 74-1057) in the hybrid (Figure 4c) are much broader compared to those observed for the precursor β-Co(OH)$_2$ (Figure 4b), suggesting increased disorder in the hydroxide rings. In addition, the peak intensity of the 001 reflection of β-Co(OH)$_2$ in the hybrid decreases drastically compared to the precursor β-Co(OH)$_2$, suggesting a reduction of platelet thickness of β-Co(OH)$_2$ due to etching.

The XRD pattern of the Co_3O_4 hexagonal ring−graphene hybrid obtained on heating β-Co(OH)$_2$ hexagonal ring−GO hybrid in air (Figure 4d) shows reflections due to spinel Co_3O_4 (JCPDS 74-2120). Peak broadening suggests that the crystallite size of the oxide is much smaller compared to that of the hydroxide rings. Broad, low-intensity 002 reflection at $2\theta = 25°$ indicates that the GO layers are reduced to graphene. Similarly, peaks due to cubic CoO (JCPDS 75-0418) and graphene are observed in the XRD pattern (Figure 4e) of the CoO hexagonal ring−graphene hybrid obtained on heating the β-Co(OH)$_2$ hexagonal ring−GO hybrid in nitrogen atmosphere. The percentages of Co_3O_4 and CoO in the corresponding metal oxide hexagonal ring−graphene hybrids were estimated to be 48 ± 2 and 43 ± 3, respectively.

The XRD patterns (Supporting Information, Figure S3) of β-$Ni_{0.33}Co_{0.67}(OH)_2$ hexagonal ring−GO and $NiCo_2O_4$ hexagonal ring−graphene hybrids confirm the conversion of the mixed metal hydroxide to the spinel oxide phase (JCPDS 73-1702). The percentage of $NiCo_2O_4$ in the $NiCo_2O_4$ hexagonal ring−graphene hybrid was determined to be 50 ± 3.

The G band (~1581 cm^{-1}) associated with the scattering of sp^2 carbon domains and disorder-related D band (~1345 cm^{-1}) in the Raman spectrum of the Co(OH)$_2$ hexagonal ring−GO (Figure 5a) and Co_3O_4 hexagonal ring−graphene (Figure 5b) hybrids are characteristic of graphene.[56,57] Decreased intensity of the defect-related D band (I_D/I_G = 0.6) in the case of Co_3O_4 hexagonal ring−graphene hybrid confirms the reduction of GO to graphene in the hybrid. The electron energy loss spectrum (EELS) of the Co_3O_4 hexagonal ring−graphene hybrid (Supporting Information, Figure S4) exhibits a peak at 286 eV due to the 1s−π* transition and another between 293 and 315 eV that correspond to the 1s−σ* transition, further supporting the presence of graphene in the hybrid.[58,59]

A detailed composition analysis of the hybrids was carried out using high-angle annular dark-field (HAADF) scanning transmission electron microscopy (STEM) and EDS elemental mapping. Figure 6a presents a HAADF STEM image of the β-Co(OH)$_2$ hexagonal ring−GO hybrid. The elemental maps of the constituting elements C, O, and Co (Figure 6b−d) clearly demonstrate a well-defined compositional profile of a β-Co(OH)$_2$ hexagonal ring in the GO matrix. Similarly, the HAADF STEM image and the elemental maps (Figure 7) confirm the compositional profile of a β-$Ni_{0.33}Co_{0.67}(OH)_2$ hexagonal ring in the GO matrix.

The peak intensities of carbonyl (C═O), hydroxyl (C−OH), and carboxylic acid (COOH) groups are relatively reduced in the core level C 1s XPS spectrum of the β-Co(OH)$_2$ hexagonal ring−GO hybrid (Figure 8b) in comparison to pristine GO (Figure 8a). This could possibly be due to the partial deoxygenation of these groups in the presence of the alkaline dispersion of β-Co(OH)$_2$ hexagonal platelets, similar to deoxygenation of GO in an alkaline solution reported in the literature.[60] While the carbonyl peak is totally absent, the peak intensities (Figure 8c) due to C−OH and COOH groups are significantly reduced in the case of Co_3O_4 hexagonal ring−graphene hybrid, indicating further reduction of GO to graphene in the hybrid. The core level Co 2p spectra (Supporting Information, Figure S5) confirm the presence of Co^{2+} of β-Co(OH)$_2$ and Co^{2+} and Co^{3+} of Co_3O_4 in the β-Co(OH)$_2$ hexagonal ring−GO and Co_3O_4 hexagonal ring−graphene hybrids, respectively.

The formation of hexagonal hydroxide rings may be explained as follows. When a hot colloidal dispersion of β-Co(OH)$_2$ hexagonal platelets (pH = 7.5) was added to the GO dispersion (pH = 3), both the layers flocculate

instantaneously to form a black product. The pH of the colorless supernatant was 6.8. The change in the pH is due to neutralization of the acidic groups on GO by the basic β-$Co(OH)_2$ hexagonal platelets. The functional groups on GO execute dual functions—anchoring the hydroxide platelets and etching them to form rings. The hexagonal hydroxide platelets are anchored to the GO layers through H-bonding interactions between the hydroxyl planes of the brucite platelets and the functional groups on GO. The H^+ ions formed due to the dissociation of the −COOH and phenolic −OH groups of GO react with the hydroxyl groups of the hydroxide platelets, causing dissolution. The central part of the hexagonal platelets is expected to be highly defective with a large extent of planar defects.[18,32] Therefore, the central core dissolves faster than the outer region. When the H^+ ions are exhausted, the dissolution of the hydroxide platelets ceases, resulting in the formation of rings. When β-$Co(OH)_2$ hexagonal platelets were reacted with graphite under similar conditions, no etching or ring formation was observed, and the platelets remained unaffected (Supporting Information, Figure S6). This further confirms the fact that the functional groups on GO layers cause the etching of the hydroxide platelets into rings.

The hybrid formation reaction was carried out targeting a 1:1 Co_3O_4−graphene hybrid, and hence a dispersion containing ~80 mg of cobalt hydroxide platelets was added to a dispersion of 200 mg of GO. In order to see if the amount of GO plays a role in the formation of metal hydroxide rings, the reaction was repeated with 100, 300, and 400 mg of GO. The amount of GO and the pH of the supernatant after flocculation of the hybrid seem to be crucial in the formation of the hybrid. The pH of the supernatant depends on the amount of GO used (Supporting Information, Table S1). When the amount of GO was decreased (100 mg), the supernatant was alkaline and the etching was not significant. The SEM image of the product (Figure 9A) shows that the hydroxide platelets have not been etched at the center. When the amount of GO was increased (300 mg), the supernatant was acidic and the platelets were etched in several regions in addition to the center (Figure 9B), resulting in perforated platelets and broken pieces. The hexagonal platelets were completely destroyed (Figure 9C) when the amount of GO was further increased to 400 mg. The reflections due to cobalt hydroxide gradually decrease in intensity and eventually are absent as the amount of GO is increased (Figure 9D), supporting the fact that the dissolution of the hydroxide platelets increases with the increase in the amount of acidic GO.

The formation of porous metal oxide rings on graphene would increase the overall exposed surface area since the inner edges of the ring along with graphene would also be available for catalytic activity. The adsorption−desorption isotherms of nitrogen at 77 K obtained using the multiple-point BET method were used to measure the surface area and pore size.

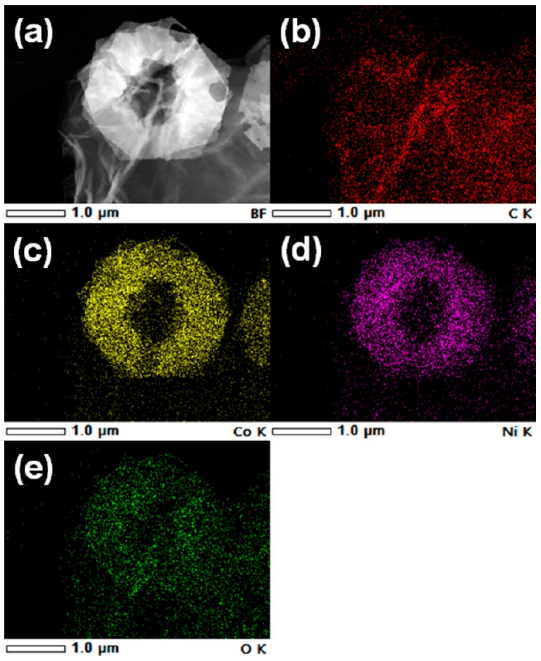

Figure 7. HAADF STEM image (a) and the spatially resolved C (b), Co (c), Ni (d), and O (e) elemental maps of the β-$Ni_{0.33}Co_{0.67}(OH)_2$ hexagonal ring−graphene oxide hybrid.

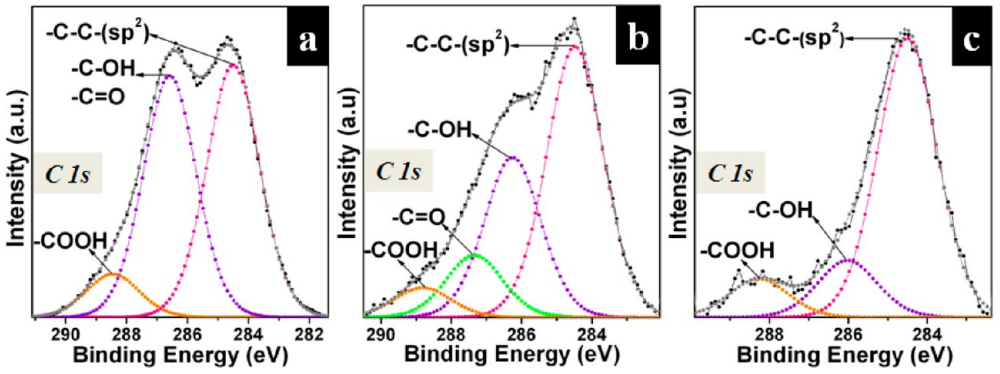

Figure 8. Core level C 1s XPS spectra of GO (a), β-$Co(OH)_2$ hexagonal ring−GO hybrid (b), and Co_3O_4 hexagonal ring−graphene hybrid (c).

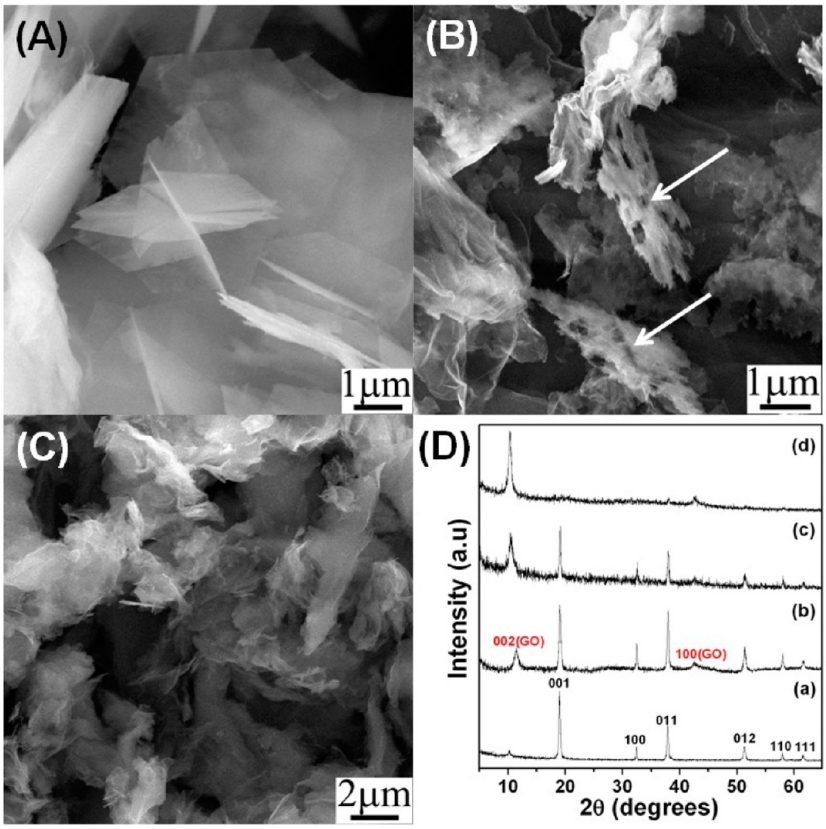

Figure 9. SEM images of β-Co(OH)$_2$ hexagonal ring−graphene oxide hybrids formed using 100 (A), 300 (B), and 400 (C) mg of GO. The arrows in (B) point to the perforated β-Co(OH)$_2$ platelets. XRD patterns (D) of β-Co(OH)$_2$ hexagonal ring−graphene oxide hybrids formed using 100 (a), 200 (b), 300 (c), and 400 (d) mg of GO.

While the specific surface area was measured using the lower part of the adsorption isotherm, desorption curve of the isotherm was used for pore size analysis. Nitrogen adsorption−desorption curves and BET surface area analysis of metal oxide−graphene hybrids are shown in Figure 10. The hybrids exhibit higher surface areas compared to pristine porous hexagonal metal oxides obtained by heating the metal hydroxide platelets in air/N_2 (Supporting Information, Figure S7).

The electrochemical performance of the samples was measured using the standard half-cell method. The cycling performance, together with the Coulombic efficiency of the Co_3O_4 hexagonal ring−graphene hybrid, is depicted in Figure 11a. The hybrid shows excellent cycle life with a stable capacity and almost 100% Coulombic efficiency. Even after 50 charge−discharge cycles, the reversible capacity of 748.3 mAhg^{-1} is retained. The achieved capacity is ~14% less than the theoretical capacity of Co_3O_4. In contrast, a commercial Co_3O_4 sample exhibits an extensive capacity fading (Figure 11a); its capacity decreased from the initial value of 1029 to 134.5 mAhg^{-1} within 20 cycles. More importantly, a Co_3O_4 hexagonal ring−graphene hybrid exhibits much improved rate capabilities (Figure 11b). A high capacity of ~585 mAhg^{-1} could be delivered even when the current density is increased to 2*C*, and a reversible capacity of 405 mAhg^{-1} could be maintained even at a much larger current density of 5*C*. The electrochemical performance is comparable to other Co_3O_4−graphene hybrids reported in the literature (Supporting Information, Table S2). These observations suggest that the unique Co_3O_4 hexagonal ring−graphene hybrid architecture is beneficial for the improvement of Co_3O_4 anode materials.

Similar results were obtained in the case of CoO hexagonal ring−graphene hybrid. Figure 11c depicts the discharge/charge capacity when cycled at a current rate of *C*/5. The first discharge capacity of the sample is larger than the theoretical value of CoO (715.4 mAhg^{-1}), which is usually attributed to irreversible reactions such as formation of a solid electrolyte interphase (SEI) layer. It is also observed that CoO hexagonal ring−graphene hybrid demonstrates much enhanced cycling performance than the commercial CoO sample.

After 50 cycles, the CoO hexagonal ring−graphene hybrid delivers a capacity of 644.5 mAhg^{-1}. The fading rate for CoO hexagonal ring−graphene hybrid is 0.7% per cycle. In contrast, fading rate for the commercial CoO samples is about 3.3%. The rate capability of the hybrid is compared with that of the commercial CoO sample in Figure 11d. It is evident that the hybrid structure exhibits much improved rate capability than the commercial CoO. Even at a high current rate of 5*C*, the CoO hexagonal ring−graphene hybrid can deliver

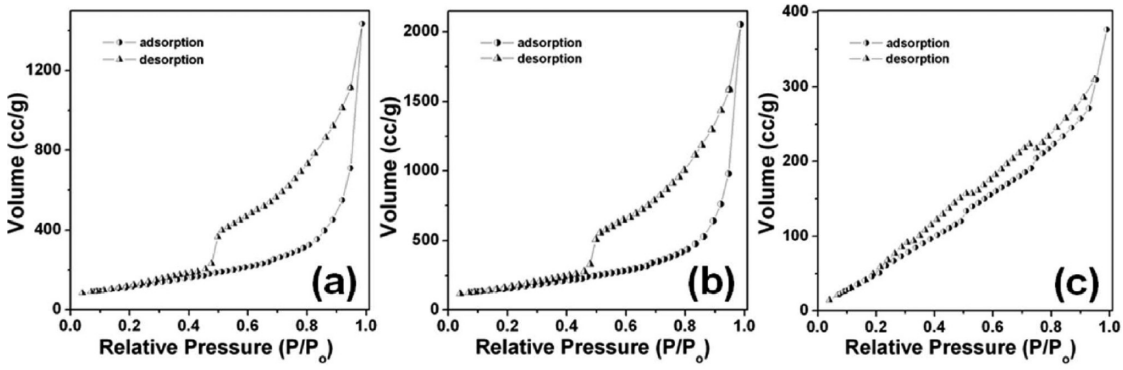

(d) hybrid	BET surface area (m^2/g)	pore volume (cc/g)	average pore diameter (Å)
Co_3O_4 hexagonal ring–graphene	429.3	2.22	206.5
CoO hexagonal ring–graphene	560.1	3.17	226.7
$NiCo_2O_4$ hexagonal ring–graphene	308.5	0.58	75.49

Figure 10. Nitrogen adsorption–desorption curves of Co_3O_4 hexagonal ring–graphene (a), CoO hexagonal ring–graphene (b), and $NiCo_2O_4$ hexagonal ring–graphene (c) hybrids. The BET surface area analysis of the hybrids is summarized in table (d).

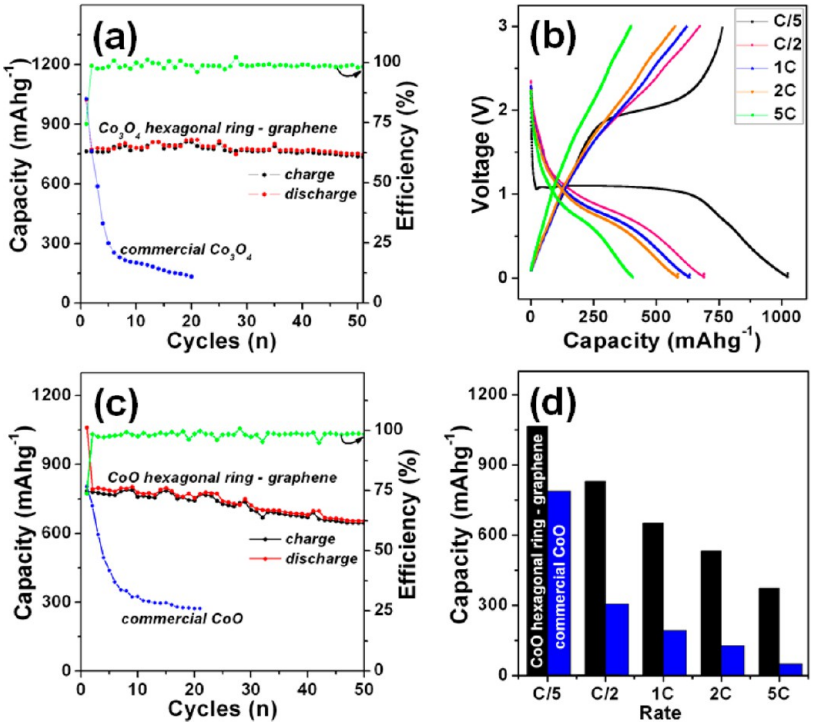

Figure 11. Cycling performance at a current density of C/5 (a) and variation of capacity delivered at different current densities of Co_3O_4 hexagonal ring–graphene (a,b) and CoO hexagonal ring–graphene (c,d) hybrids, respectively. The capacities are based on the masses of the hybrids.

a capacity of 373.1 mAhg^{-1} while the commercial CoO exhibited only 42.8 mAhg^{-1} at 5C. The electrochemical performance is comparable to other CoO–graphene hybrids reported in the literature (Supporting Information, Table S3).

The superior electrochemical performances of porous Co_3O_4 and CoO hexagonal ring–graphene hybrids originate from their unique structural features. First, the conductivity of the hybrids would be dramatically enhanced due to the presence of graphene. Therefore,

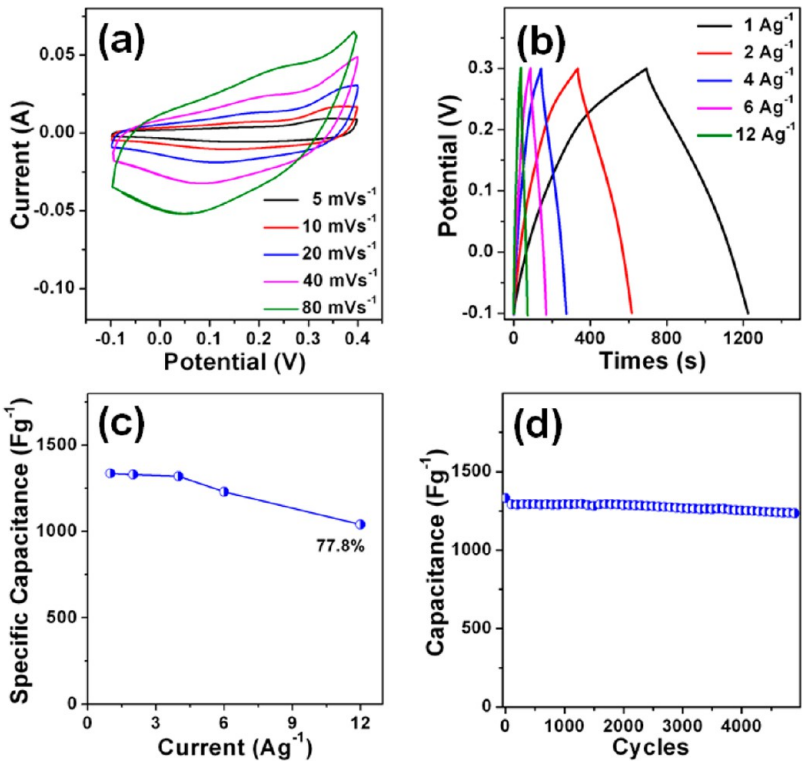

Figure 12. (a) Cyclic voltammograms at different scan rates, (b) charge−discharge curves at different current densities, (c) specific capacitance at various current densities, and (d) cycling performance of the $NiCo_2O_4$ hexagonal ring−graphene hybrid.

the electronic transport length (L_e) in the hybrids would be effectively shortened compared to pure Co_3O_4 and CoO nanocrystals, leading to reduced particle−particle interface resistance. Second, the nanopores in the oxide rings can effectively buffer the volume changes during lithiation/delithiation. Hence the problem of pulverization of the electrode materials is greatly alleviated, and the cycling performance is remarkably improved. Third, the thin nanorings (~15 nm) not only render a short transport length for Li^+ during charging/discharging but also enhance the surface area, favoring a high rate performance. Fourth, the crystal plane effect also plays an important role. The SAED patterns of the hybrids (Figure 3d and Supporting Information, Figure S2) suggest that (111) planes are dominantly exposed in the porous oxide rings, which results in more cobalt atoms on the surfaces of Co_3O_4 crystals when compared with (001) planes. According to literature, 1.875 Co^{2+} belongs to (111) facets, while only 1 Co^{2+} is found in the (001) facet.[61,62] The synergetic effects of high conductivity of hybrid, small diffusion lengths in thin rings and nanoporous surface that buffers the volume expansion unique to the porous Co_3O_4 and CoO hexagonal ring−graphene hybrids are responsible for the excellent electrochemical performance of the electrodes.

The $NiCo_2O_4$ ring−graphene hybrid exhibits excellent electrochemical performance as a supercapacitor electrode (Figure 12). Figure 12a shows the cyclic voltammetry (CV) curves of the hybrid electrodes measured in a 5 M NaOH aqueous electrolyte solution at various scan rates ranging from 5 to 80 mV s^{-1}. The lack of symmetry in the curves is due to pseudocapacitance behavior. Broad redox peaks within −0.1 to 0.4 V (*vs* standard calomel electrode, SCE) are observed in all CV curves. These are mainly attributed to the Faradaic redox reactions related to M−O/M−O−OH (M = Ni or Co). The redox peaks could be observed even at a very high scan rate of 80 mV s^{-1}. Figure 12b depicts the charge−discharge behavior of the $NiCo_2O_4$ ring−graphene hybrid between −0.1 and 0.3 V at various current densities ranging from 1 to 12 Ag^{-1}. All the charge−discharge curves are nearly symmetric in shape, revealing good capacitive behavior and electrochemical reversibility. Figure 12c illustrates the current density dependence of the capacitance of the hybrid. The hybrid shows a high capacitance of 1337 Fg^{-1} at 1 Ag^{-1}. A specific capacitance of 1230 Fg^{-1} is delivered even when the current density is increased by 4 times to 4 Ag^{-1}. When the discharge current was enhanced to 12 Ag^{-1}, the $NiCo_2O_4$ ring−graphene hybrid showed 77.8% retention of the capacitance. This further demonstrates that $NiCo_2O_4$ hexagonal ring−graphene hybrid architecture and the porous surface of the oxide rings play a positive role in the overall supercapacitor performance. In addition, the $NiCo_2O_4$ hexagonal ring−graphene hybrid exhibited high cyclic stability. Only

a small loss of capacitance (less than 7%) was detected after 5000 charge−discharge cycles (Figure 12d). Therefore, owing to the highly nanoporous surface and thin nanorings, the $NiCo_2O_4$ hexagonal ring−graphene hybrid exhibited not only high capacitance but also long cycling stability, which are the key parameters for commercial applications in high-demand energy storage. The specific capacitance of $NiCo_2O_4$ hexagonal ring−graphene hybrid is better than the hybrids with other morphologies of $NiCo_2O_4$ reported in the literature (Supporting Information, Table S4).

The large improvement in the capacitance of the $NiCo_2O_4$ ring−graphene hybrid could be attributed to synergy effects of thin nanorings, nanoporous surfaces, and graphene support. Graphene in the hybrid contributes to high conductivity, while the nanoporous surface (BET surface area 308.5 $m^2\ g^{-1}$, Figure 10) increases the available electroactive surface area. Moreover, the nanopores of the nanorings would not only serve as a robust reservoir for ions, leading to greatly improved diffusion kinetics within the electrode, but also ensure efficient contact between the surface of the electroactive rings and the electrolyte even at high rates. In addition, the interaction between conductive graphene with each $NiCo_2O_4$ nanoring with good intrinsic electrical conductivity supports fast electron transport leading to high rate capability.

CONCLUSION

We demonstrate that the mildly acidic GO layers can be used as etchants to convert hexagonal metal hydroxide nanoplatelets into hexagonal rings. Using GO layers as etchants is advantageous as the nanorings formed are hybridized with GO layers. These hybrids, on heating, yield porous metal oxide nanoring−graphene hybrids. The unique metal oxide nanoring−graphene architecture exhibits enhanced electrochemical performance in energy storage applications. This method could be extended to other preformed nanostructures. It could also promote the development of novel functional graphene hybrids.

METHODS

Synthesis of GO. The method of Hummers and Offeman[63] was adopted to prepare GO from graphite powder. About 1 g of graphite powder was added to 23 mL of cold (0 °C) concentrated H_2SO_4. About 3 g of $KMnO_4$ was added gradually under stirring and cooling, so that the temperature of the mixture was maintained below 20 °C. The mixture was then stirred at 35 °C for 30 min. About 46 mL of distilled water was slowly added to increase the temperature to 98 °C, and the mixture was maintained at this temperature for 15 min. The reaction was terminated by adding 140 mL of distilled water followed by the addition of 10 mL of 30% H_2O_2 solution. The solid product was separated by centrifugation, washed repeatedly with 5% HCl solution until sulfate could not be detected with $BaCl_2$, then washed 3−4 times with acetone and dried in an air oven at 65 °C overnight.

Synthesis of β-$Co(OH)_2$ Hexagonal Platelets. β-$Co(OH)_2$ hexagonal platelets were synthesized as reported in the literature.[64] First, 0.237 g of $CoCl_2 \cdot 6H_2O$ and 1.68 g of hexamethylenetetramine (HMT) were dissolved in 200 cm^3 of a 9:1 mixture of deionized water and ethanol. The mixture was heated at 90 °C for 1 h. The product was recovered by centrifuging, washed with water, and dried at 65 °C overnight. Typical yield of the platelets is ~80 mg.

Synthesis of β-$Co(OH)_2$ Hexagonal Ring−GO Hybrid. GO (200 mg) was dispersed in 400 mL of water by sonication for 1 h (pH = 3). Then, 200 mL of the pink colored colloidal dispersion of β-$Co(OH)_2$ hexagonal platelets obtained in the previous step (90 °C, pH = 7.5) was added to the GO dispersion with constant stirring. The stirring was continued for a further 10 min. Immediate flocculation was observed. The settled black precipitate was washed repeatedly with water−ethanol mixture and dried at room temperature.

Synthesis of Co_3O_4/CoO Hexagonal Ring−Graphene Hybrids. β-$Co(OH)_2$ hexagonal ring−GO hybrid was heated in air or N_2 at 500 °C for 5 h.

Synthesis of $NiCo_2O_4$ Hexagonal Ring−GO Hybrid. β-$Ni_{0.33}Co_{0.67}(OH)_2$ hexagonal platelets were synthesized as reported in literature.[65] $CoCl_2 \cdot 6H_2O$ (0.237 g), $NiCl_2 \cdot 6H_20$ (0.118 g), and HMT (1.26 g) were dissolved in 200 mL of water, and the mixture was refluxed for 5 h with stirring under a N_2 blanket. β-$Ni_{0.33}Co_{0.67}(OH)_2$ hexagonal platelets were reacted with graphene oxide as explained in the case of synthesis of β-$Co(OH)_2$ hexagonal ring−GO hybrid. The resulting sample was heated in air at 500 °C for 5 h to obtain $NiCo_2O_4$ hexagonal ring−graphene hybrid.

Electrochemical Studies. *Lithium-Ion Battery.* For electrochemical measurement, the samples were initially heated at 80 °C under vacuum for 5 h to remove adsorbed water. Active material (80 wt %), polyvinylidenedifluoride (10 wt %), and acetylene black (10 wt %) were mixed and ground to a consistent paste. The working electrode was prepared by pressing the paste on a 0.25 cm^2 Cu mesh (100 mesh). The working electrode was dried under vacuum to constant weight. Lithium metal pressed on Cu mesh was used as reference and counter electrodes. $LiClO_4$ (1 M) in ethyl carbonate (EC)−diethyl carbonate (DEC) mixture (EC/DEC = 1:1 v/v) was used as electrolyte. Cell assembly was carried out in a glovebox under an argon atmosphere. The charge−discharge performance of the material was investigated in such three-electrode cell using lithium metal as counter and reference electrodes, similar to the procedure reported in literature.[66] Galvanostatic discharge−charge studies were carried out in a potential range of 50 mV to 3.0 V (Li^+/Li) at different current densities. The electrochemical measurements were normalized to the mass of the active material (Co_3O_4/CoO hexagonal ring−graphene hybrid or commercial Co_3O_4/CoO). Reproducibility of the electrochemical data was confirmed by repeating the experiments with at least another electrode of the same sample.

Supercapacitor. The electrochemical properties of the $NiCo_2O_4$ hexagonal ring−graphene hybrid were measured using a Solartron electrochemical workstation. The standard three-electrode cell was composed of SCE as a reference electrode, Pt mesh as a counter electrode, and the synthesized composite sample as the working electrode, respectively. A 5 M NaOH solution served as electrolyte at room temperature. Cyclic voltammetry was analyzed at various scan rates (5−80 mV/s). Galvanostatic charge/discharge curves were obtained at various current densities of 1−12 A/g to evaluate the specific capacitance. The loading mass of active materials in the electrode was ~2−4 mg/cm^2 for the supercapacitor and Li-ion battery measurements.

Characterization. All the samples were characterized by powder X-ray diffraction (XRD) using a Philips X'pert Pro diffractometer (Cu Kα radiation, secondary graphite monochromator, 2° 2θ per min). Transmission electron microscopy (TEM) images were recorded using a JEOL-3000F microscope operated at 300 kV. Scanning electron microscopy (SEM) images were recorded on a Hitachi S4800 electron microscope operating at

15 kV. X-ray photoelectron spectroscopy (XPS) measurements were carried out with an ESCALab220i-XL spectrometer using a twin-anode Al Kα (1486.6 eV) X-ray source. All spectra were calibrated to the binding energy of the C 1s peak at 284.51 eV. The base pressure was around 3×10^{-7} Pa. Raman spectra were recorded on a Horiba Jobin-Yvon T6400 Raman spectrometer. The nitrogen physisorption isotherms were recorded at 77 K on a Quantachrome Autosorb-1 system after outgassing of samples at 150 °C for 24 h. The metal contents of the samples were estimated by ion chromatography using a Metrohm 861 advanced compact ion chromatograph with Metrosep C 250 cation column and conductivity detector.

Conflict of Interest: The authors declare no competing financial interest.

Acknowledgment. The authors thank Drs. Yamada, K. Iiyama, A. Nukui, and M. Mitome for their generous technical assistance. This work was funded by the World Premier International Center for Materials Nanoarchitectonics (WPI-MANA) of NIMS, Tsukuba, Japan. C.R.R. and M.R. acknowledge the funding of this work by DST, India (SR/S1/PC-23/2011).

Supporting Information Available: SEM and TEM images, XRD, EELS, XPS, and BET analysis of cobalt-based hydroxide/oxide hexagonal ring−graphene hybrids. This material is available free of charge *via* the Internet at http://pubs.acs.org.

REFERENCES AND NOTES

1. Puntes, V. F.; Krishnan, K. M.; Alivisatos, A. P. Colloidal Nanocrystal Shape and Size Control: The Case of Cobalt. *Science* **2001**, *291*, 2115–2117.
2. Manna, L.; Milliron, D. J.; Meisel, A.; Scher, E. C.; Alivisatos, A. P. Controlled Growth of Tetrapod-Branched Inorganic Nanocrystals. *Nat. Mater.* **2003**, *2*, 382–385.
3. Yin, Y.; Rioux, R. M.; Erdonmez, C. K.; Hughes, S.; Somorjai, G. A.; Alivisatos, A. P. Formation of Hollow Nanocrystals through the Nanoscale Kirkendall Effect. *Science* **2004**, *304*, 711–714.
4. Lim, B.; Xia, Y. Metal Nanocrystals with Highly Branched Morphologies. *Angew. Chem., Int. Ed.* **2011**, *50*, 76–85.
5. Chen, H.; Kou, X.; Yang, Z.; Ni, W.; Wang, J. Shape- and Size-Dependent Refractive Index Sensitivity of Gold Nanoparticles. *Langmuir* **2008**, *24*, 5233–5237.
6. Nethravathi, C.; Sen, S.; Ravishankar, N.; Rajamathi, M.; Pietzonka, C.; Harbrecht, B. Ferrimagnetic Nanogranular Co_3O_4 through Solvothermal Decomposition of Colloidally Dispersed Monolayers of α-Cobalt Hydroxide. *J. Phys. Chem. B* **2005**, *109*, 11468–11472.
7. Nethravathi, C.; Machado, J.; Gautam, U. K.; Avadhani, G. S.; Rajamathi, M. Exfoliation of Copper Hydroxysalt in Water and the Conversion of the Exfoliated Layers to Cupric and Cuprous Oxide Nanoparticles. *Nanoscale* **2012**, *4*, 496–501.
8. Zinchenko, A. A.; Yoshikawa, K.; Baigl, D. DNA-Templated Silver Nanorings. *Adv. Mater.* **2005**, *17*, 2820–2823.
9. Sun, Y.; Xia, Y. Triangular Nanoplates of Silver: Synthesis, Characterisation and Use as Sacrificial Templates for Generating Triangular Nanorings of Gold. *Adv. Mater.* **2003**, *15*, 695–699.
10. Jiang, L.-P.; Xu, S.; Zhu, J.-M.; Zhang, J.-R.; Zhu, J.-J.; Chen, H.-Y. Ultrasonic-Assisted Synthesis of Monodisperse Single-Crystalline Silver Nanoplates and Gold Nanorings. *Inorg. Chem.* **2004**, *43*, 5877–5883.
11. Métraux, G. S.; Cao, Y. C.; Jin, R.; Mirkin, C. A. Triangular Nanoframes Made of Gold and Silver. *Nano Lett.* **2003**, *3*, 519–522.
12. Liusman, C.; Li, S.; Chen, X.; Wei, W.; Zhang, H.; Schatz, G. C.; Boey, F.; Mirkin, C. A. Free-Standing Bimetallic Nanorings and Nanoring Arrays Made by On-Wire Lithography. *ACS Nano* **2010**, *4*, 7676–7682.
13. Fan, N.; Yang, Y.; Wang, W.; Zhang, L.; Chen, W.; Zou, C.; Huang, S. Selective Etching Induces Selective Growth and Controlled Formation of Various Platinum Nanostructures by Modifying Seed Surface Free Energy. *ACS Nano* **2012**, *6*, 4072–4082.
14. Halpern, A. R.; Corn, R. M. Lithographically Patterned Electrodeposition of Gold, Silver, and Nickel Nanoring Arrays with Widely Tunable Near-Infrared Plasmonic Resonances. *ACS Nano* **2013**, *7*, 1755–1762.
15. Zhu, F. Q.; Fan, D. L.; Zhu, X. C.; Zhu, J. G.; Cammarata, R. C.; Chien, C. I. Ultrahigh-Density Arrays of Ferromagnetic Nanorings on Macroscopic Areas. *Adv. Mater.* **2004**, *16*, 2155–2159.
16. Guo, L.; Liang, F.; Wang, N.; Kong, D.; Wang, S.; He, L.; Chen, C.; Meng, X.; Wu, Z. Preparation and Characterization of Ring-Shaped Co Nanomaterials. *Chem. Mater.* **2008**, *20*, 5163–5168.
17. Hu, M.-J.; Lu, Y.; Zhang, S.; Guo, S.-R.; Lin, B.; Zhang, M.; Yu, S.-H. High Yield Synthesis of Bracelet-like Hydrophilic Ni-Co Magnetic Alloy Flux-Closure Nanorings. *J. Am. Chem. Soc.* **2008**, *130*, 11606–11607.
18. Li, F.; Ding, Y.; Gao, P.; Xin, X.; Wang, Z. L. Single-Crystal Hexagonal Disks and Rings of ZnO: Low-Temperature, Large-Scale Synthesis and Growth Mechanism. *Angew. Chem., Int. Ed.* **2004**, *43*, 5238–5242.
19. Wang, X.; Xi, G.; Xiong, S.; Liu, Y.; Xi, B.; Yu, W.; Qian, Y. Solution-Phase Synthesis of Single-Crystal CuO Nanoribbons and Nanorings. *Cryst. Growth Des.* **2007**, *7*, 930–934.
20. Yi, D. K.; Kim, D.-Y. Novel Approach to the Fabrication of Macroporous Polymers and Their Use as a Template for Crystalline Titania Nanorings. *Nano Lett.* **2003**, *3*, 207–211.
21. Shen, G.; Chen, D. Self-Coiling of $Ag_2V_4O_{11}$ Nanobelts into Perfect Nanorings and Microloops. *J. Am. Chem. Soc.* **2006**, *128*, 11762–11763.
22. Xu, C.-Y.; Liu, Y.-Z.; Zhen, L.; Wang, Z. L. Disket−Nanorings of $K_2Ti_6O_{13}$ Formed by Self-Spiraling of a Nanobelt. *J. Phys. Chem. C* **2008**, *112*, 7547–7551.
23. Hu, X.; Yu, J. C.; Gong, J.; Li, Q.; Lia, G. α-Fe_2O_3 Nanorings Prepared by a Microwave-Assisted Hydrothermal Process and Their Sensing Properties. *Adv. Mater.* **2007**, *19*, 2324–2329.
24. Jia, C.-J.; Sun, L.-D.; Luo, F.; Han, X.-D.; Heyderman, L. J.; Yan, Z.-G.; Yan, C.-H.; Zheng, K.; Zhang, Z.; Takano, M.; *et al.* Large-Scale Synthesis of Single-Crystalline Iron Oxide Magnetic Nanorings. *J. Am. Chem. Soc.* **2008**, *130*, 16968–16977.
25. Paek, J.; Lee, C. H.; Choi, J.; Choi, S.-Y.; Kim, A.; Lee, J. W.; Lee, K. Gadolinium Oxide Nanoring and Nanoplate: Anisotropic Shape Control. *Cryst. Growth Des.* **2007**, *7*, 1378–1380.
26. Yan, C.; Singh, N.; Lee, P. S. Kinking-Induced Structural Evolution of Metal Oxide Nanowires into Single-Crystalline Nanorings. *ACS Nano* **2010**, *4*, 5350–5356.
27. Duan, J. H.; Yang, S. G.; Liu, H. W.; Gong, J. F.; Huang, H. B.; Zhao, X. N.; Tang, J. L.; Zhang, Z.; Du, Y. W. AlN Nanorings. *J. Cryst. Growth* **2005**, *283*, 291–296.
28. Jian, J. K.; Zhang, Z. H.; Sun, Y. P.; Lei, M.; Chen, X. L.; Wang, T. M.; Wang, C. GaN Nanorings: Another Example of Spontaneous Polarization-Induced Nanostructure. *J. Cryst. Growth* **2007**, *303*, 427–432.
29. Liu, B.; Zeng, H. C. Semiconductor Rings Fabricated by Self-Assembly of Nanocrystals. *J. Am. Chem. Soc.* **2005**, *127*, 18262–18268.
30. Chen, J.; Liao, W.-S.; Chen, X.; Yang, T.; Wark, S. E.; Son, D. H.; Batteas, J. D.; Cremer, P. S. Evaporation-Induced Assembly of Quantum Dots into Nanorings. *ACS Nano* **2009**, *3*, 173–180.
31. Han, Q.; Yuan, Y.; Liu, X.; Wu, X.; Bei, F.; Wang, X.; Xu, K. Room-Temperature Synthesis of Self-Assembled Sb_2S_3 Films and Nanorings *via* a Two-Phase Approach. *Langmuir* **2012**, *28*, 6726–6730.
32. Wang, W.; Long, D.; Liang, Y.; Zhang, G.; Zeng, B.; He, Q. Conversion of Hexagonal Sb_2Te_3 Nanoplates into Nanorings Driven by Growth Temperature. *Langmuir* **2011**, *27*, 815–819.
33. Cho, K.-S.; Talapin, D. V.; Gaschler, W.; Murray, C. B. Designing PbSe Nanowires and Nanorings through Oriented Attachment of Nanoparticles. *J. Am. Chem. Soc.* **2005**, *127*, 7140–7147.
34. Xin, G.-Q.; Ding, H.-P.; Yang, Y.-G.; Shen, S.-L.; Xiong, Z.-C.; Chen, X.; Hao, J.; Liu, H.-G. Triangular Single-Crystalline

Nanorings of PbS Formed at the Air/Water Interface. *Cryst. Growth Des.* **2009**, *9*, 2008–2012.
35. Guo, Q.; Kim, S. J.; Kar, M.; Shafarman, W. N.; Birkmire, R. W.; Stach, E. A.; Agrawal, R.; Hillhouse, H. W. Development of $CuInSe_2$ Nanocrystal and Nanoring Inks for Low-Cost Solar Cells. *Nano Lett.* **2008**, *8*, 2982–2987.
36. Hu, P.; Pramana, S. S.; Cao, S.; Ngaw, C. K.; Lin, J.; Loo, S. C. J.; Tan, T. T. Y. Ion-Induced Synthesis of Uniform Single-Crystalline Sulphide-Based Quaternary-Alloy Hexagonal Nanorings for Highly Efficient Photocatalytic Hydrogen Evolution. *Adv. Mater.* **2013**, *25*, 2567–2572.
37. Chun, H.; Hahm, M. G.; Homma, Y.; Meritz, R.; Kuramochi, K.; Menon, L.; Ci, L.; Ajayan, P. M.; Jung, Y. J. Engineering Low-Aspect Ratio Carbon Nanostructures: Nanocups, Nanorings, and Nanocontainers. *ACS Nano* **2009**, *3*, 1274–1278.
38. Iyer, K. S.; Saunders, M.; Becker, T.; Evans, C. W.; Raston, C. L. Nanorings of Self-Assembled Fullerene C_{70} as Templating Nanoreactors. *J. Am. Chem. Soc.* **2009**, *131*, 16338–16339.
39. Miao, J.-J.; Fu, R.-L.; Zhu, J.-M.; Xu, K.; Zhu, J.-J.; Chen, H.-Y. Fabrication of $Cd(OH)_2$ Nanorings by Ultrasonic Chiselling on $Cd(OH)_2$ Nanoplates. *Chem. Commun.* **2006**, 3013–3015.
40. Shen, Y.; Yin, J.; Gao, F.; Wang, J.; Pangb, H.; Lub, Q. One-Step Fabrication of $Cd(OH)_2$ Nanorings *via* a Solution Phase Synthesis. *Chem. Commun.* **2010**, *46*, 6183–6185.
41. Rothman, J.; Klaui, M.; Lopez-Diaz, L.; Vaz, C. A. F.; Bleloch, A.; Bland, J. A. C.; Cui, Z.; Speaks, R. Observation of a Bi-domain State and Nucleation Free Switching in Mesoscopic Ring Magnets. *Phys. Rev. Lett.* **2001**, *86*, 1098–1101.
42. Zhu, F. Q.; Chern, G. W.; Tchernyshyov, O.; Zhu, X. C.; Zhu, J. G.; Chien, C. L. Magnetic Bistability and Controllable Reversal of Asymmetric Ferromagnetic Nanorings. *Phys. Rev. Lett.* **2006**, *96*, 27205–27209.
43. Zhu, J.-G.; Zheng, Y. F.; Prinz, G. A. Ultrahigh Density Vertical Magnetoresistive Random Access Memory. *J. Appl. Phys.* **2000**, *87*, 6668–6673.
44. Aizpurua, J.; Hanarp, P.; Sutherland, D. S.; Kall, M.; Bryant, G. W.; de Abajo, F. J. G. Optical Properties of Gold Nanorings. *Phys. Rev. Lett.* **2003**, *90*, 057401–057404.
45. Martel, R.; Shea, H. R.; Avouris, P. Rings of Single-Walled Carbon Nanotubes. *Nature* **1999**, *398*, 299.
46. Kong, X. Y.; Ding, Y.; Yang, R.; Wang, Z. L. Single-Crystal Nanorings Formed by Epitaxial Self-Coiling of Polar Nanobelts. *Science* **2004**, *303*, 1348–1351.
47. Croft, R. C. Lamellar Compounds of Graphite. *Quart. Rev.* **1960**, *14*, 11–13.
48. Szabó, T.; Berkesi, O.; Forgó, P.; Josepovits, K.; Sanakis, Y.; Petridis, D.; Dékány, I. Evolution of Surface Functional Groups in a Series of Progressively Oxidized Graphite Oxides. *Chem. Mater.* **2006**, *18*, 2740–2749.
49. Szabó, T.; Tombácz, E.; Illés, E.; Dekany, I. Enhanced Acidity and pH-Dependent Surface Charge Characterization of Successively Oxidized Graphite Oxides. *Carbon* **2006**, *44*, 537–545.
50. Wang, H.; Robinson, J. T.; Diankov, G.; Dai, H. Nanocrystal Growth on Graphene with Various Degrees of Oxidation. *J. Am. Chem. Soc.* **2010**, *132*, 3270–3271.
51. Guo, S.; Dong, S.; Wang, E. Three-Dimensional Pt-on-Pd Bimetallic Nanodendrites Supported on Graphene Nanosheet: Facile Synthesis and Used as an Advanced Nanoelectrocatalyst for Methanol Oxidation. *ACS Nano* **2010**, *4*, 547–555.
52. Nethravathi, C.; Viswanath, B.; Michael, J.; Rajamathi, M. Hydrothermal Synthesis of a Monoclinic VO_2 Nanotube–Graphene Hybrid for Use as Cathode Material in Lithium Ion Batteries. *Carbon* **2012**, *50*, 4839–4846.
53. Liu, M.; Lu, Y.; Chen, W. PdAg Nanorings Supported on Graphene Nanosheets: Highly Methanol-Tolerant Cathode Electrocatalyst for Alkaline Fuel Cells. *Adv. Funct. Mater.* **2013**, *23*, 1289–1296.
54. Luo, B.; Liu, S.; Zhi, L. Chemical Approaches toward Graphene-Based Nanomaterials and Their Applications in Energy-Related Areas. *Small* **2012**, *8*, 630–646.
55. Ma, R.; Osada, M.; Hu, L.; Sasaki, T. Self-Assembled Nanofilm of Monodisperse Cobalt Hydroxide Hexagonal Platelets: Topotactic Conversion into Oxide and Resistive Switching. *Chem. Mater.* **2010**, *22*, 6341–6346.
56. Malard, L. M.; Pimenta, M. A.; Dresselhaus, G.; Dresselhaus, M. S. Raman Spectroscopy in Graphene. *Phys. Rep.* **2009**, *473*, 51–87.
57. Ferrari, A. C.; Meyer, J. C.; Scardaci, V.; Casiraghi, C.; Lazzeri, M.; Mauri, F.; Piscanec, S.; Jiang, D.; Novoselov, K. S.; Roth, S.; *et al.* Raman Spectrum of Graphene and Graphene Layers. *Phys. Rev. Lett.* **2006**, *97*, 187401–187405.
58. Suenaga, K.; Sandre, E.; Colliex, C.; Pickard, C. J.; Kataura, H.; Iijima, S. Electron Energy-Loss Spectroscopy of Electron States in Isolated Carbon Nanostructures. *Phys. Rev. B* **2001**, *63*, 165408–165414.
59. Alexandrou, I.; Scheibe, H.-J.; Kiely, C. J.; Papworth, A. J.; Amaratunga, G. A. J.; Schultrich, B. Carbon Films with an sp^2 Network Structure. *Phys. Rev. B* **1999**, *60*, 10903–10907.
60. Fan, X.; Peng, W.; Li, Y.; Li, X.; Wang, S.; Zhang, G.; Zhang, F. Deoxygenation of Exfoliated Graphite Oxide under Alkaline Conditions: A Green Route to Graphene Preparation. *Adv. Mater.* **2008**, *20*, 1–4.
61. Xiao, X.; Liu, X.; Zhao, H.; Chen, D.; Liu, F.; Xiang, J.; Hu, Z.; Li, Y. Facile Shape Control of Co_3O_4 and the Effect of the Crystal Plane on Electrochemical Performance. *Adv. Mater.* **2012**, *24*, 5762–5766.
62. Liu, D.; Wang, X.; Wang, X.; Tian, W.; Bando, Y.; Golberg, D. Co_3O_4 Nanocages with Highly Exposed {110} Facets for High-Performance Lithium Storage. *Sci. Rep.* **2013**, *3*, 2543–2549.
63. Hummers, W. S.; Offeman, R. E. Preparation of Graphite Oxide. *J. Am. Chem. Soc.* **1958**, *80*, 1339.
64. Liu, Z.; Ma, R.; Osada, M.; Takada, K.; Sasaki, T. Selective and Controlled Synthesis of α- and β-Cobalt Hydroxides in Highly Developed Hexagonal Platelets. *J. Am. Chem. Soc.* **2005**, *127*, 13869–13874.
65. Liang, J.; Ma, R.; Iyi, N.; Ebina, Y.; Takada, K.; Sasaki, T. Topochemical Synthesis, Anion Exchange, and Exfoliation of Co-Ni Layered Double Hydroxides: A Route to Positively Charged Co-Ni Hydroxide Nanosheets with Tunable Composition. *Chem. Mater.* **2010**, *22*, 371–378.
66. Zhou, H.; Li, D.; Hibino, M.; Honma, I. A Self-Ordered, Crystalline-Glass, Mesoporous Nanocomposite for Use as a Lithium-Based Storage Device with Both High Power and High Energy Densities. *Angew. Chem., Int. Ed.* **2005**, *44*, 797–802.